Published in Physical Review Letters 41, issue 17, 11760-11769, 1990
which should be used for any reference to this work

L and *M* edges of copper: Theory and experiment

P. Aebi,* M. Erbudak, F. Vanini, D. D. Vvedensky,† and G. Kostorz
Institut für Angewandte Physik, Eidgenössische Technische Hochschule Zürich, CH-8093 Zürich, Switzerland

Characteristic electronic transitions and the associated fine structure in the near-edge region are investigated with electron-energy-loss spectroscopy for the copper *L* and *M* edges. In a single-particle scattering picture this fine structure represents the unoccupied density of states selected by the matrix elements. However, electronic processes can often complicate this simple approach. In order to test the applicability of this model, full multiple-scattering calculations within a real-space formalism are presented and compared with measurements. An expression is derived and implemented in order to include excitations described by the first Born approximation for the initial and final states of the primary electron. Calculating the generalized oscillator strengths shows that different core edges of Cu behave differently with regard to the dipole selection rules. Some edges favor dipole-allowed transitions at large momentum transfer, while others show dipole-forbidden transitions even at small momentum transfer.

I. INTRODUCTION

The development of methods based on scattering-state fine structures is driven mainly by the need for structural methods which permit the investigation of the geometrical environment of different atomic species of the sample. Therefore one is tempted to apply an extended x-ray-absorption fine-structure (EXAFS) analysis to extract neighbor distances as soon as structures that resemble oscillations due to interference of scattering states are observed. However, electronic processes often are complicated to the extent that a simple scattering picture breaks down.

In the following structures originating from scattering states observed in electron spectroscopy from solid surface are investigated. The aim of this work is to perform electron-energy-loss experiments *and* calculations in order to examine how far a scattering picture is applicable. Computations give the possibility of a direct comparison between theory and experiment, as well as the ability to estimate the relative strengths of transition probabilities to the various channels.

Experimentally the effort is focused on the attainment of the highest possible signal-to-background ratio. Sometimes this ratio is as low as 10^{-4} at threshold. The fine structures above the edge are smaller again approximately by a factor of 10. Thus, the main problem is to achieve simultaneously good statistics, high resolution, and reasonable measuring times.

In an electron-energy-loss experiment primary electrons of a given energy are directed at a sample, and the backscattered secondary electrons are analyzed in energy and intensity. In the range of energies from 100 to 3000 eV the analyzed region of the sample comprises a depth of a few atomic layers. In a single-particle picture the primary electrons can either be scattered elastically, resulting in a diffraction pattern from a single-crystal surface and/or undergo an inelastic process. Elastic scattering is basis of low-energy electron diffraction[1] where electron energies up to 300 eV are used. This work concentrates on inelastic processes which create a core hole.

The time scale plays an important role in the excitation process. In the sudden approximation the surrounding electron shells do not feel that an electron has been excited above the Fermi level E_F, and there is no relaxation during the process, i.e., the overlap between the excited state and possible decay channels is small. In the so-called adiabatic approximation the outer electron shells relax and can partially impart their relaxation energy to the excited photoelectron. Unlike photons, primary electrons can give an arbitrary part of their energy to a core electron. In the sudden approximation this means that in measuring the energy loss of a primary electron and considering a certain core level, one knows how far above E_F the core electron has been excited. In this case the core electron makes a transition into a delocalized scattering state. The spectrum above the edge thus represents an angular momentum projected empty density of states (DOS) following the symmetry of the final state. On the other hand, depending on the symmetry, the final state can be completely localized [e.g., La $4d$-$4f$ (Ref. 2) and $3d$-$4f$ (Ref. 3) transitions] so that it does not interact with the solid at all and final-state multiplets are measured. In this case the scattering picture must be replaced by a full atomic-configuration-based approach.[4]

Other complications occur for almost perfect overlap between the initial core state and a state that could fill the core hole in an Auger process.[5] In this case excitation and relaxation happen on the same time scale. The situation becomes dynamical to the extent that a single-particle picture is no longer appropriate, and excitation and relaxation are no longer separable. Other complications occur when different excitation channels that lead to decay to the same final state have a large overlap integral. A Fano-like broadening[6] then appears because one has to account for interference between these channels.

Electron-energy-loss spectroscopy (EELS) yields infor-

mation on the initial and final states and the matrix elements coupling them. Hence, such experiments need the support of the theoretical DOS and the transition-matrix elements that weight the transitions to different angular momentum channels. For the excitation of core states, mainly the unoccupied DOS has been investigated; modulations measured above the core edges are the basis of x-ray-absorption near-edge structure (XANES) and EXAFS used for the structural investigation of the local environment of atoms in a solid. Owing to the increasing mean free path of the electrons excited above E_F and the more isotropic scattering factors in going from the EXAFS to the XANES regime, interference between the incoming and outgoing electron waves is due not only to single backscattering by neighboring atoms of the excited atom, but also to scattering by several centers, i.e., multiple scattering (MS). For the excitation of the inner shells, mostly x rays from a synchrotron-radiation source have been used. EXAFS-like modulations have also been reported in EELS with high-energy electrons (300 keV) (Ref. 17) in transmission and with low-energy (1–2 keV) (Ref. 8) electrons in reflection experiments.

The extended fine structures of the Cu $3p$ edge, within the simple EXAFS analysis,[9] yield a prominent peak which, apart from a phase-shift correction, is directly related to the nearest-neighbor distance. It is exactly this phase-shift correction which gave rise to considerable debate[8,10,11] because a discrepancy exists between crystallographic nearest-neighbor distances and those derived from conventional EXAFS analysis. The same problem occurs for other $M_{2,3}$ edges of transition metals.[8] If, in the single-scattering analysis, one uses calculated $p \rightarrow \varepsilon d$ ionization phase shifts, the nearest-neighbor distance obtained is systematically 0.2–0.3 Å smaller than the crystallographic value. This was suggested to be the result of inaccurate $p \rightarrow \varepsilon d$ ionization phase shifts, although essentially the same result is obtained if one uses $2p \rightarrow \varepsilon d$ (Ref. 12) or $3p \rightarrow \varepsilon d$ (Ref. 10) calculated phase shifts. Phase shifts were also calculated for Cu in the $Z+1$ and in the relaxed, empty-$3p$ approximations,[10] but this did not give a significant improvement. Tran Thoai *et al.*[13] have proposed that the error arises from the omission of $3p \rightarrow \varepsilon s$ excitations and that it could be compensated by an empirical k-dependent ratio for the εd and εs transitions. In fact, some years ago Lytle *et al.*[14] proposed that the non-Gaussian line shapes observed in the Fourier transform of the $L_{2,3}$ EXAFS spectrum of high-Z elements arises from a non-negligible $p \rightarrow \varepsilon s$ contribution. However, Rabe *et al.*[15] convincingly demonstrated that the non-Gaussian shape is the result of an oscillation in the backscattering amplitude. This supports the assumption that $p \rightarrow \varepsilon s$ contributions can be neglected in an EXAFS analysis. In order to further investigate this point Combet Farnoux and Hitchcock[11] examined a single-particle calculation of the $3p \rightarrow \varepsilon s$ and $3p \rightarrow \varepsilon d$ atomic ionization cross sections for some $3d$ transition elements. These calculations do not support the explanation of Tran Thoai *et al.*[13] because the εs channel is stronger than εd only in a very limited energy range. So the question remains as to the origin of the systematic error in the $M_{2,3}$ extended fine-structure analysis. The problem seems to be associated with the $M_{2,3}$ ionization since De Crescenzi *et al.*[8] and Fanfoni *et al.*[16] have shown that the same discrepancy arises in the analysis of the $M_{2,3}$ EXAFS, obtained with photon rather than electron impact ionization.

To investigate this problem further and to rule out that the simplification of the EXAFS analysis may be responsible for it, we have performed electron-energy-loss measurements on the Cu $2p$, $3s$, and $3p$ edges, which are compared with multiple-scattering calculations for the excitation spectra. Included in the theoretical analysis is an explicit evaluation of the matrix element for different angular momentum final states without invoking the dipole selection rule. This feature of our analysis turns out to be important since some levels show dipole-forbidden transitions even in the limit of small-momentum transfer.

The outline of this paper is as follows. In Sec. II the experimental setup is described. Section III develops the theoretical approach, with specific attention on the calculation of the matrix element for the transition probabilities. The results of the measurements and the calculations are presented in Sec. IV, with conclusions and summary in Sec. V.

II. EXPERIMENT

The measurements were performed in a ultrahigh-vacuum (UHV) apparatus with a total pressure in the 10^{-8} Pa range. A copper single-crystal surface was oriented with the x-ray Laue method and electropolished. In UHV, the surface was cleaned by etching with Ar^+ and heating to 900 K until no traces of O, C, and Ar were detectable by Auger-electron spectroscopy. Surfaces thus prepared delivered sharp LEED patterns. Spectra were recorded with a Riber Mac-2 energy analyzer. In this analyzer the energy analysis of the electrons, focused by an input lens, is obtained by combining a two-grid retarding stage with a dispersive energy filter. The energy resolution is constant over the whole energy range and was chosen between 0.4 and 0.75 eV.

Detection of the secondary electrons was in all cases achieved with a high-current Channeltron coupled to a low-noise operational current amplifier with an amplification of 10^8 which floats on a positive high voltage. The signal was separated from the high voltage by means of an optocoupler, then fed to a voltage-to-frequency converter whose output was connected to a counter. The advantage of the voltage-to-frequency converter is that data are accumulated during the whole measuring time and not only at one time as it is the case with an analog-to-digital converter. But the crucial point is that the voltage-to-frequency converter has a resolution of 10^6 per 10 V and not only 13 to 16 bits (binary digits) as for an analog-to-digital converter. Data collection and the energy sweep of the analyzer were controlled by a Digital Equipment Corporation PDP-11 microcomputer. The data acquisition time was several hours for the electron-energy-loss near-edge measurements.

III. THEORY

Throughout this work the muffin-tin model is used according to the Mattheiss prescription[17] for the potential.

The atoms of the solid are surrounded by contiguous spheres. The charge density of the crystal is constructed by superposing atomic charge densities from self-consistent calculations,[18,19] with only the spherical part retained within the sphere surrounding each atom. The Poisson equation is then solved in order to calculate the Coulomb potential; the exchange potential is calculated within a Slater $X\alpha$ prescription.[20] Once this potential is constructed, the Schrödinger equation can be integrated within the muffin-tin sphere of the atom at site j for any positive energy E to calculate the phase shifts $\delta_l(E)$ and wave functions $R_l^j(r,E)$ for angular momentum l. Here $R_l^j(r,E)$ is the radial solution for the single muffin-tin potential at site j matching on the free solution

$$R_l^j(r,E)=j_l(\sqrt{E}\,r)\cos\delta_l^j-n_l(\sqrt{E}\,r)\sin\delta_l^j$$

outside the muffin-tin, and j_l (n_l) is the usual spherical Bessel (Neumann) function.

To calculate the transition probabilities of the various excitation channels, we apply the Fermi golden rule of first-order time-dependent perturbation theory:

$$W=\frac{2\pi}{\hbar}\sum_s |M_{E_s,\mathbf{p}_s}^{E_{\rm inc},\mathbf{p}_{\rm inc}}|^2\delta(E_{\rm inc}+E_i-E_f-E_s)\ , \qquad (1)$$

where the subscript "inc" denotes quantities for the initial state of the primary electron, i for the initial core state, f for the final state of the primary electron after inelastic scattering, and s for a scattering state of the photoelectron. Without allowing for exchange,[21–23] the matrix elements are given by

$$M_{E_s,\mathbf{p}_s}^{E_{\rm inc},\mathbf{p}_{\rm inc}}=\int d\mathbf{r}_1\int d\mathbf{r}_2\psi_f^*(\mathbf{r}_1)\psi_{\rm inc}^*(\mathbf{r}_2)V\psi_f(\mathbf{r}_2)\psi_s(\mathbf{r}_1)\ , \qquad (2)$$

where V is an unscreened Coulomb interaction:

$$V=V(\mathbf{r}_1,\mathbf{r}_2)=\frac{1}{|\mathbf{r}_1-\mathbf{r}_2|}\ ,$$

and the charge e has been set to unity.

Taking plane waves for the initial and final states of the primary electron (Born approximation[24]),

$$\psi_{\rm inc}=e^{i\mathbf{q}_i\cdot\mathbf{r}},\quad \psi_f=e^{i\mathbf{q}_f\cdot\mathbf{r}}\ ,$$

we show in the Appendix that Eq. (1) can be written in the form

$$W=-\frac{2}{\hbar}\int d\mathbf{r}_1\cdots\int d\mathbf{r}_2'\psi_i^*(\mathbf{r}_1)\frac{1}{|\mathbf{r}_1-\mathbf{r}_2|}e^{i(\mathbf{q}_f-\mathbf{q}_i)\cdot\mathbf{r}_2}\times{\rm Im}G^+(\mathbf{r}_1,\mathbf{r}_1';E_{\rm inc}+E_i-E_f)\times e^{-i(\mathbf{q}_f-\mathbf{q}_i)\cdot\mathbf{r}_2'}\frac{1}{|\mathbf{r}_1'-\mathbf{r}_2'|}\psi_i(\mathbf{r}_1')\ , \qquad (3)$$

where $G^+(\mathbf{r}_1,\mathbf{r}_1';E)$ is the Green's function at energy E of the scattering photoelectron:[25,26]

$$G^+(\mathbf{r},\mathbf{r}';E)=G_a^+(\mathbf{r},\mathbf{r}';E)+k\sum_{L,L'}R_l(r,E)Y_L(\hat{\mathbf{r}})\frac{\tau_{LL'}^{00}(E)-it_L^0(E)\delta_{LL'}}{\sin\delta_l(E)\sin\delta_{l'}(E)}R_{l'}(r',E)Y_{L'}(\hat{\mathbf{r}}')\ . \qquad (4)$$

Here, $k=\sqrt{E}$, Y_L ($L=\{l,m\}$) is a spherical harmonic, $\hat{\mathbf{r}}$ denotes azimuthal and polar angles of $\mathbf{r}$, and t_l^0 is the reflection coefficient of the Lth partial wave at energy E given in terms of the phase shifts $\delta_l(E)$ by $t_l^0(E)=\frac{1}{2}(e^{2i\delta_l(E)}-1)$. The quantities $\tau_{LL'}^{00}(E)$ are matrix elements of the scattering path operator τ which sums all paths that begin and end at the site of the excited atom in angular momentum states L and L', respectively, and G_a^+ is the atomic Green's function,

$$G_a^+(\mathbf{r},\mathbf{r}';E)=-ik\sum_L R_l(r_<,E)R_l^+(r_>,E)Y_L(\hat{\mathbf{r}})Y_L(\hat{\mathbf{r}}')\ , \qquad (5)$$

where $R_l(r,E)$ [$R_l^+(r,E)$] is the regular (irregular) solution of the radial Schrödinger equation for the single muffin-tin potential of the excited atom.

Substituting $\mathbf{q}=\mathbf{q}_f-\mathbf{q}_i$, fixing $\mathbf{r}_1$ and $\mathbf{r}_1'$ (for $\mathbf{r}_2$ and $\mathbf{r}_2'$ integrations), defining

$$\mathbf{r}_2=\mathbf{r}_1+\mathbf{r}\rightarrow d\mathbf{r}_2=d\mathbf{r}\ ,\quad \mathbf{r}_2'=\mathbf{r}_1'+\mathbf{r}\rightarrow d\mathbf{r}_2'=d\mathbf{r}'\ ,$$

and using the angular expansion of G^+ around the site of excitation, which is possible because of the localized nature of the core function, ψ_i, one finally obtains

$$W=-\frac{32\pi^2}{\hbar q^4}k\left[\sum_L|M_{i,L}|^2-{\rm Im}\sum_{L,L'}M_{i,L}\frac{\tau_{LL'}^{00}(E_s)-it_L^0(E_s)\delta_{LL'}}{\sin\delta_l(E_s)\sin\delta_{l'}(E_s)}M_{i,L'}^*\right]\ , \qquad (6)$$

where

$$M_{i,L}=\int d\mathbf{r}\,\psi_i^*(\mathbf{r})e^{i\mathbf{q}\cdot\mathbf{r}}\psi_L(\mathbf{r})\ ,$$

with $\psi_i(\mathbf{r})=R_{l_i}(r,E_i)Y_{L_i}(\hat{\mathbf{r}})$ and $\psi_L(\mathbf{r})=R_L(r,E_s)Y_L(\hat{\mathbf{r}})$. The transition probability is represented by a term due to the atom and another due to the solid. The latter allows for interference between outgoing and incoming angular momentum states.

We should remark at this point that the general form of (6) is appropriate in more general settings whenever the mag-

nitude of the matrix element is appreciable only within a particular muffin-tin sphere. For example, a recent application to bremsstrahlung isochromat spectroscopy (BIS) (Ref. 27) uses equations and techniques formally identical to those described here.

To calculate the matrix element $M_{i,L}$ we invoke

$$e^{i\mathbf{q}\cdot\mathbf{r}}=4\pi\sum_{l=0}^{\infty}\sum_{m=-l}^{l} i^l(-1)^m j_l(qr)Y_{l,-m}(\hat{\mathbf{r}})Y_{l,m}(\hat{\mathbf{q}})$$

to obtain

$$M_{i,L'}=4\pi\sum_{l=0}^{\infty} i^l\int_0^{\infty} dr\, R_i^*(r)j_l(qr)R_{l'}(r)\sum_{m=-l}^{l}(-1)^{m+m_i}Y_L(\hat{\mathbf{q}})\int d\Omega\, Y_{l_i,-m_i}(\hat{\mathbf{r}})Y_{l,-m}(\hat{\mathbf{r}})Y_{l',m'}(\hat{\mathbf{r}})\ . \tag{7}$$

The quantity W is a transition probability per unit time. What must be compared with experiment is the number of transitions per unit time per unit energy for the experimental conditions, i.e., the differential cross section. In an experiment, a primary beam of electrons has a wave vector $\mathbf{k}_i$, and the final state of the primary electrons is given by $\mathbf{k}_f$. These two vectors define

$$\mathbf{q}=\mathbf{k}_i-\mathbf{k}_f\ , \tag{8}$$

the momentum transfer. In our experiment we are integrating over all angles. In almost every case the primary electrons undergo elastic backscattering (either before or after inelastic scattering) to come out of the solid, so we consider one inelastic event and one or more elastic events. This means that we have incident primary electrons from every direction with respect to the site of the inelastic event and that the directions of $\mathbf{k}_i$ and $\mathbf{k}_f$ are not fixed. For this reason, we have to integrate over all possible incident directions or, because scattering depends only on the momentum transfer (8), over all possible directions of $\mathbf{q}$. We have seen above [Eq. (6)] that

$$q_{\min}=k_i-k_f\ , \tag{9}$$

the minimal momentum transfer for a given energy loss, gives the most important contribution.

From (8) we have

$$q^2=k_i^2+k_f^2-2k_ik_f\cos\theta_{if} \tag{10}$$

and

$$q\,dq=k_ik_f\sin\theta_{if}d\theta_{if}\ , \tag{11}$$

where θ_{if} is the angle between $\mathbf{k}_i$ and $\mathbf{k}_f$. Expressed in terms of W, the differential cross section is given by

$$\frac{\partial\sigma^2}{\partial\Omega_f\partial E}d\Omega_f=\frac{W}{j_i}dv_f \tag{12}$$

with Ω_f the solid angle of $\mathbf{k}_f$, j_i the incident particle current density, and dv_f the differential phase-space element around $\mathbf{k}_f$. Neglecting the prefactors we obtain

$$\frac{\partial\sigma^2}{\partial\Omega_f\partial E}d\Omega_f\propto W\frac{k_f}{k_i}d\Omega_f\ . \tag{13}$$

Using (11) and the fact that $d\Omega_f=\sin\theta_{if}d\phi_id\theta_{if}$, where ϕ_i is the angle around $\mathbf{k}_i$, this becomes

$$\frac{\partial\sigma^2}{\partial_q\partial E}dq\propto\int_0^{2\pi}d\phi_i\,W\frac{q}{k_i^2}dq\propto\int_0^{2\pi}d\phi_i\,Wq\,dq\ . \tag{14}$$

Note that $W=W(\mathbf{q})$ depends on the orientation of $\mathbf{q}$ with respect to the sample and that for a given direction of $\hat{\mathbf{k}}_i$ and $\hat{\mathbf{k}}_f$ (i.e., in an angle-resolved experiment) the direction and the absolute value of $\mathbf{q}$ varies with the change of energy loss $\Delta E=E_f-E_i$. However for a narrow energy range (in the near-edge region) $\mathbf{q}$ may be considered as constant.

From (14) and (6) we see that the differential cross section goes as q^{-3} so that its value is much larger for small q. Consequently $q_{\min}$, the minimal momentum transfer for a given energy loss, gives the most important contribution. Therefore the quantity to compare with experiment is

$$\int d\Omega\frac{\partial\sigma^2}{dq\,\partial E}\propto\int Wq\,d\Omega_i=\int Wq\,d\Omega_q \tag{15}$$

where $d\Omega_q$ is the solid angle of $\mathbf{q}$.

The quantities that are necessary for the calculation are τ^{00}, $\delta_l(E)$, $R_l(r,E)$, and $M_{i,L}$. Phase shifts and continuum wave functions are produced with a muffin-tin program that solves the Schrödinger equation. Phase shifts and continuum wave functions for each energy are then used as input to a modified version of ICXANES (Ref. 28) to calculate the l-projected local DOS and the τ^{00} matrix for every energy. The multiple-scattering calculations were performed on a Cray Research Inc. X-MP/28 supercomputer.

IV. RESULTS

To investigate the excitation process, we first calculate the quantity

$$\frac{E}{q^2}|\langle L|e^{i\mathbf{q}\cdot\mathbf{r}}|i\rangle|^2 \tag{16}$$

which is proportional to the projected generalized oscillator strength (GOS),[29] so-called because of its similarity with the optical oscillator strength in the zero-q limit. In (16) $E=E_i-E_f$ is the energy loss and $\mathbf{q}=\mathbf{q}_i-\mathbf{q}_f$ is the momentum transfer. As a function of q and E, (16) is also known as the "Bethe surface."[30]

Figure 1 shows the GOS for the ionization of a Cu $3p$ core level. The momentum transfer $\mathbf{q}$ is fixed in the z

direction. The total GOS is the sum over the GOS for $l=0$, 1, 2, and 3 final states. The figures labeled s,p,d,f show the behavior of the l-projected GOS as a function of energy and momentum transfer. For comparison of the absolute magnitude a plot is made for $q=10^{-4}$ a.u., i.e., the dipole case [q(a.u.)$=\sqrt{2E\,(\text{hartree})}=0.529\ q(\text{Å}^{-1})$, a_0=Bohr radius $=0.529$ Å, 1 hartree$=27.2$ eV]. It shows that dipole-allowed transitions are strongest for $q_{\min}$ but dipole-forbidden transitions can be of the same strength for larger q values. For transitions to d symmetry a characteristic minimum is present. This is due to the extinction of the radial integral when the nodes of the Bessel function with q and those of the final-state wave function with E move through the overlap area of the core wave function. For small q and E the $3p$-to-s transition is almost as strong as the $3p$-to-d transition, but then it decreases rapidly with q and E. Transitions to p symmetry have their maximum for q values around 2–4 a.u. for increasing energy up to 12.5 hartree. The same occurs for the $3p$-to-f transitions, which is very strong in the specific q and E range. For $q=1.5$ a.u. and $q=3$ a.u., we see that the GOS is dominated by transitions to p and f symmetries, respectively.

In Fig. 2 the Cu $3p3s$ spectrum is plotted (upper curve). Primary electrons of 2060 eV were used. A cubic spline is already subtracted for eliminating the background of secondary electrons. The $3p$ edge rises at 1986.5 eV, corresponding to an energy loss of 73.5 eV. A weak shoulder in the rise is attributed to the $3p_{1/2}$-$3p_{3/2}$ splitting of 1.5 eV. The $3s$ edge occurs at 1937.9 eV, i.e., at an energy loss of 120.1 eV. The lower curve in Fig. 2 is the computed $3p$ excitation with the computed $3s$ excitation multiplied by a factor of 5. The calculation was performed with a cluster appropriate for bulk Cu with a lattice constant of 3.615 Å. A bulk instead of a surface cluster is used because of a better agreement of the $2p$ edge (see below). Convergence in angular momentum and cluster size was achieved by considering atoms up to a distance of 7.2 Å from the excited atom and angular momentum phase shifts up to $l=3$. An energy independent imaginary part of the potential of 1 eV was taken into account for lifetime broadening. The cross section was computed for $q_{\min}=0.23$ a.u., integrated over $d\Omega_q$. An integration over q from $q_{\min}$ to 6 a.u. had almost no effect on the structures in the calculation. First of all one notes the steep increase of the background on the high-energy side of the $3p$ edge. Of course this steepness depends strongly on the background subtraction, but the results are reminiscent of a Fano-type broadening and asymmetry as reported in Refs. 31 and 32. Furthermore, the intensity ratio between the $3s$ and $3p$ excitation edge is far too strong compared with the calculated ratio.

Comparing structures of the computed curve with the

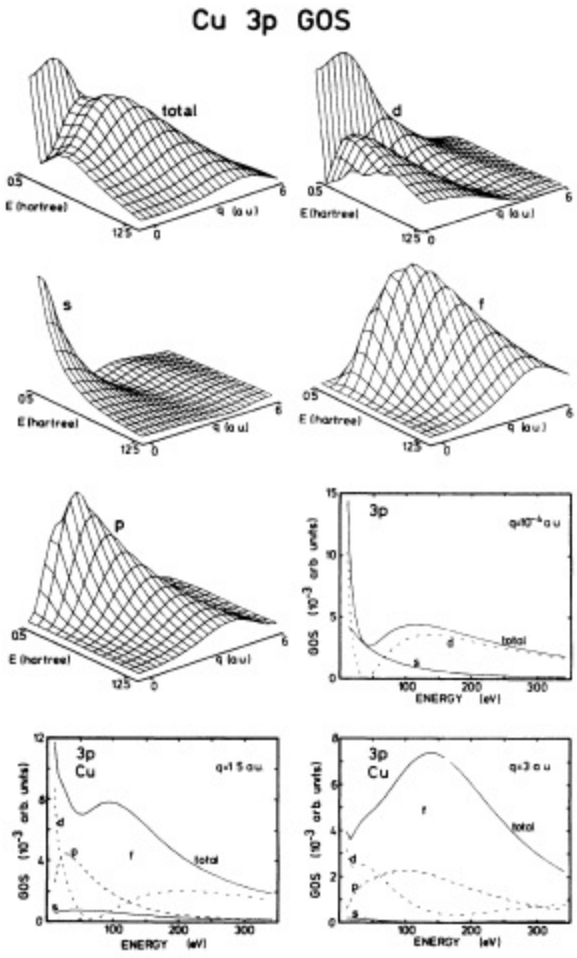

FIG. 1. Survey of the $3p$ GOS: plots labeled s,p,d,f show contributions to different final-state symmetries summed up to the total GOS. For comparison of the absolute magnitudes, a two-dimensional graph shows the contribution for the dipole case as a function of energy. For $q=1.5$ and $q=3$ a.u. contributions with p and f final-state symmetries are strongest.

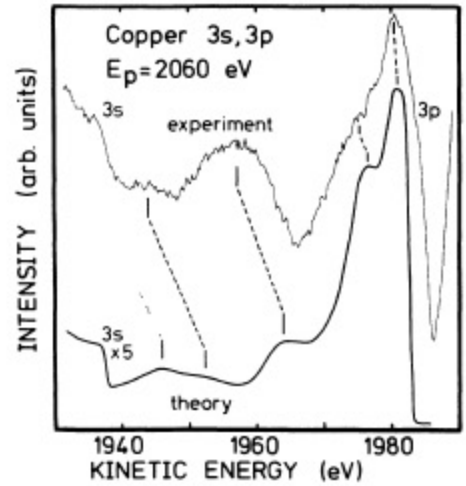

FIG. 2. The $3p3s$-loss spectrum (upper curve) after subtraction of a cubic spline. The primary energy was 2060 eV. The lower curve shows the calculated $3p$ cross section with the $3s$ contribution times 5, shifted by 45 eV. A tentative assignment of corresponding features in the experimental and theoretical curves is represented by the dashed lines.

measurement we see that common features exist, but only in a narrow energy range near the $3p$ threshold. If the structures at higher energies are of the same origin, then this suggests an energy-dependent effect. In order to emphasize this fact, corresponding features in the experimental and theoretical curves are indicated and connected by dashed lines. Such an energy-dependent effect is certainly related to the finding that in the EXAFS analysis of the Cu $3p$ edge the value for the nearest-neighbor distance is not completely independent on the k range transformed. Different energy scales for calculations and experiment were already described in BIS measurements.[33] There the authors report that the discrepancy between BIS and DOS does not vary linearly with kinetic energy. They propose for the theoretical description, to use an energy-dependent rather than an energy-independent potential, although the energy-dependent potentials calculated within the free-electron-gas model[34] do not fully describe this behavior. Another unknown influence are fine structures due to the $3d$ edge. A calculation of the $3d$ GOS shows that it is stronger than the $3p$ GOS by a factor of 10. Furthermore, if the $3p$ loss is too weak, owing to dynamical processes which do not allow a separation of excitation and relaxation, the situation is definitely uncertain.

Turning to the $3s$ edge, Fig. 3 shows the GOS for the excitation of the $3s$ level. In general the magnitude is smaller by a factor of 10 than the $3p$ excitation owing to the different symmetry of the initial state. Again dipole-allowed transitions are strongest for small q values and dipole-forbidden ones are strong for high-q values. The plots for $q=1.5$ and 3 a.u. allow us to compare the magnitude of the different transitions. Figure 4 shows the $3s$ edge on an enhanced scale (upper curve). It was measured under the same conditions as the preceding $3p$ spectrum. Comparison with theory is rendered more difficult by the uncertainty of the influence of the $3d$ and $3p$ edges. The lower curve is the calculated cross section integrated from $q_{\min}=0.36$ to 6 a.u. and over $d\Omega_q$. Common features are in very good agreement. This is surprising because the calculation does not take into account the other edges. Either structures from other edges ($3p, 3d$) are flat in this energy range or structures observed in the extended energy region originate from the $3s$ edge. This point should be investigated further. Trying to consider the influence of the $3p$ edge makes the agreement poor.

In performing the MS calculation of the cross section of the $3p$ and $3s$ edge of Cu we see that fine structures from interfering scattering paths are present but that the energy scales of theory and experiment do not fit together owing to the fast decay process of the $3p$ hole. In fact, the excitation of the $3p$ edge calls for a dynamical treatment considering coherently the fast $3p3d3d$ super-Coster-Kronig transition via which the $3p$ hole decays.

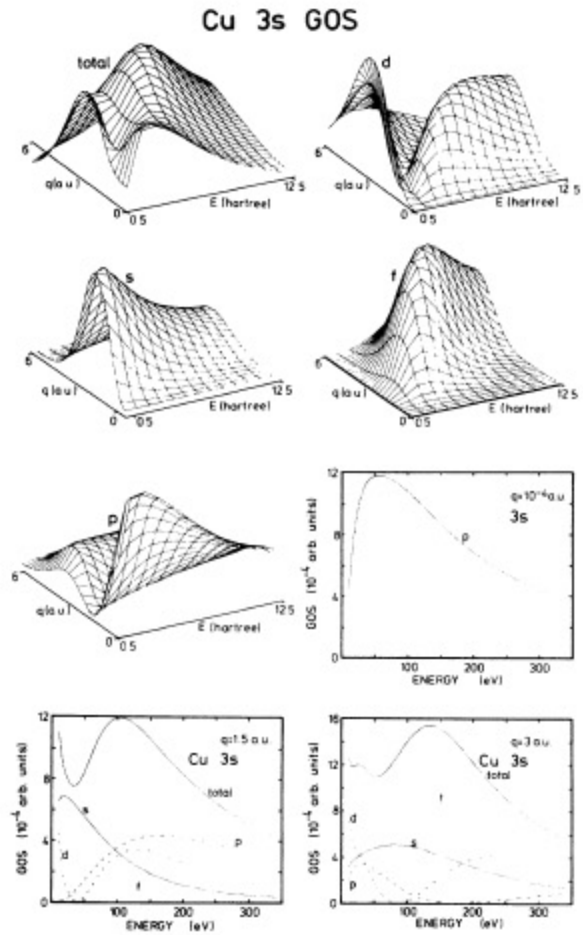

FIG. 3. A survey of the $3s$ GOS: plots labeled s,p,d,f show contributions to different final-state symmetries summed up to the total GOS. For comparison of the absolute magnitudes, a two-dimensional graph shows the contribution for the dipole case as a function of energy. For $q=1.5$ and $q=3$ a.u. contributions with s, d, and f final-state symmetries become stronger with increasing q and energies larger than 50 eV.

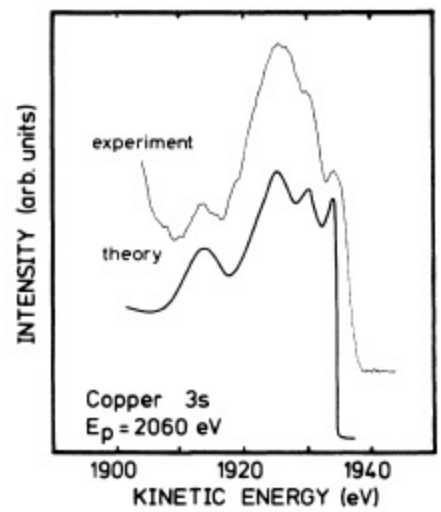

FIG. 4. The $3s$-loss spectrum (upper curve) after subtraction of a linear function. The lower curve displays the cross section for $q_{\min}=0.36$ a.u.

Furthermore the measured 3*s*-to-3*p* excitation cross-section ratio is found to be much stronger than the calculated one. This again points to electronic processes that are not fully understood. But in any case the validity of applying a simple EXAFS analysis above the 3*p* edge without considering the 3*d* and 3*s* excitation contributions is doubtful without investigating the strength of the different contributions. It would be a fortunate coincidence that both contributions are in phase and reduce the attenuation of the structures.

Figure 5 shows the GOS for the ionization of the 2*p* level. As in the case of 3*p* and 3*s* the curves labeled *s*,*p*,*d*,*f* represent the *l*-projected GOS. For three different fixed *q* values the GOS is plotted as a function of energy. It is remarkable that even at large *q* values the overall dominance of transitions into *d*-type final-state symmetry remains. At $q = 3$ a.u., *p*- and *f*-type final-state symmetries increase to values larger than the dipole-allowed *s*-type final state, but are still much smaller than transitions to *d* symmetry. The difference between the behavior of the 3*p* and 2*p* GOS occurs because of the different core wave functions. The 2*p* orbital is located closer to the nucleus so that the overlap with continuum wave functions other than those with *d* symmetry is small for the energies observed.

The fact that transitions to *d*-type continuum states are so strong, even at a high momentum transfer, would explain the perfect agreement between an experiment using high-energy electrons in an electron microscope (see Ref. 35) and that with electrons of a primary energy of 2915 eV in reflection mode from the point of view of dipole selection rules that are fulfilled even at high momentum transfer (Fig. 6). This figure shows the experiment (upper curve) and the calculated cross section (lower curve). The model cluster was a bulklike cluster as described before. Excitation spectra calculated with the (100) surface, the excitation site in the surface layer, does not reproduce the first little structure after the leading edge at 1979 eV. In traveling to a deeper layer this structure is reproduced to increasingly better degree. This shows in a convincing way that the features produced by the electrons with a kinetic energy of about 2000 eV do not mainly originate from the surface layer. The explanation for the good agreement between the transmission experiment and that in reflection mode is thus based on two arguments. First, the dipole selection rule is fulfilled for both experiments and secondly, the presented experiment in reflection mode is sensitive to bulk properties.

The extended fine structures above the 2*p* edges are shown in Fig. 7. The upper curve is the negative second derivative reflection energy-loss spectrum from Ref. 36 recorded with a primary energy of 2400 eV. It is in good agreement with the photoabsorption experiment of Ref.

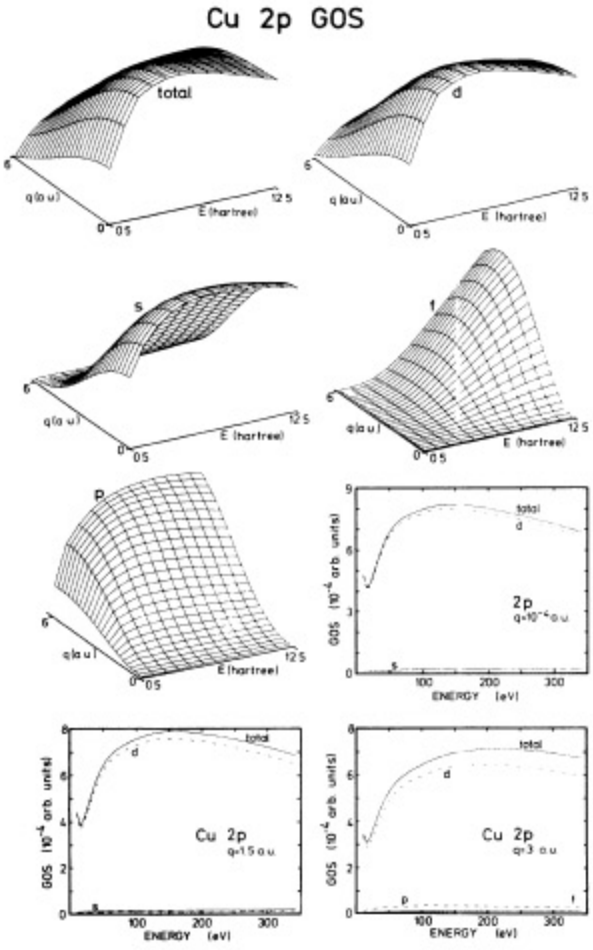

FIG. 5. Survey of the 2*p* GOS: plots labeled *s*,*p*,*d*,*f* show contributions to different final-state symmetries summed up to the total GOS. For comparison of the absolute magnitudes, a two-dimensional graph shows the contribution for the dipole case as a function of energy. For $q = 1.5$ and $q = 3$ a.u. contributions with *d* final-state symmetry stay strongest.

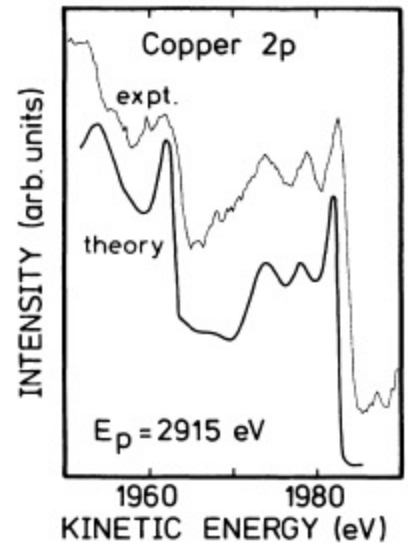

FIG. 6. Upper curve: The energy distribution of backscattered electrons of a primary energy of 2915 eV in the region of the characteristic energy loss of the Cu $2p_{1/2}$ and $2p_{3/2}$ levels. Lower curve: calculated cross section.

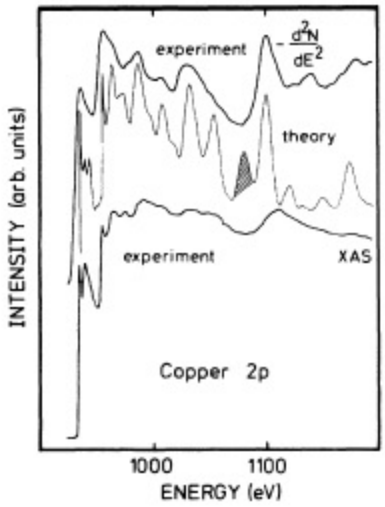

FIG. 7. Comparison between reflection energy loss in the negative second derivative mode with a primary energy of 2400 eV (Ref. 36) (upper curve), theory (middle curve), and photoabsorption (x-ray-absorption spectroscopy) (Ref. 37).

37 (lower curve) and the calculated cross section for a bulklike cluster (middle curve). The agreement between the results of the two experiments can be explained by the same arguments as before. For the calculation, the same spectra were added with a ratio of 2:1 for $2p_{3/2}$ and $2p_{1/2}$, respectively, shifted according to their binding energies. The contributions from $2p_{3/2}$ and $2p_{1/2}$ turn out to be more or less in phase, so that extinction effects are attenuated. Comparison between experiment and theory shows good agreement, apart from the shaded peak (see also Ref. 38). We have used the original ICXANES routine[28] to calculate the 1*s*-excitation spectrum of Cu in an extended region. The results are shown in Fig. 8 along with the x-ray-absorption data.[39] Except for a minor difference between the experimental and theoretical curves around 9090 eV, there is an overall agreement

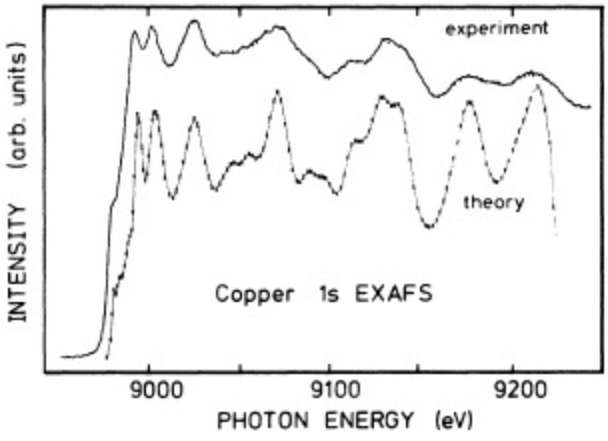

FIG. 8. Comparison of measured Cu 1*s* EXAFS (Ref. 39) with a MS calculation with the program ICXANES (Ref. 28).

concerning the energy values and the relative intensities of the modulations.

So far only excitation processes have been observed, but it is worth noting that relaxations also show an interesting behavior. A detailed discussion of the 2*s*-, 2*p*-, 3*s*-, and 3*p*-*VV* Auger relaxation is given in Ref. 40 and references therein.

V. CONCLUSION

Fine structures observed in secondary-electron and energy-loss spectra from a copper surface have been presented. Calculations were performed, computing the excitation within Fermi's golden rule and considering full multiple scattering for the secondary electron.

Comparison of the calculated generalized oscillator strength and of the cross sections with the electron-energy-loss spectra shows that the different core levels behave very differently: There are levels which favor dipole-allowed transitions even at large momentum transfer and in turn others allow for dipole-forbidden transitions already at relatively small q value. An integration over the absolute value of the momentum transfer for the computation of the cross section is therefore necessary in order to achieve agreement between experiment and computation.

In the region of the shallow core levels attention has to be paid to the relative influence of edges that are closely spaced on the energy scale. In addition, electronic effects are disturbing the scattering picture, for instance, in Cu 3*p*. Therefore, for investigations of the local environment, it is important to test the suitability of different edges of a given species. In copper the 3*s* edge follows well and the 2*p* edges follow very well the model of delocalized scattering states excited by a primary electron. For the 2*p* edge, however, a bulk cluster model explains the experiment better than a (100)-surface cluster. This shows that not only the surface layer contributes absorber atom sites, but to a considerably larger extent deeper-lying layers intervene.

Owing to the property of the method to test the local environment of the absorber, it averages over all possible absorber site environments. Hence, for the study of an adsorbate at the surface it may be better to investigate the environment of the adsorbate. Difficulties can occur if the concentration is low and/or the scattering is weak. But the method should be applicable for the study of adsorption of species at a unique site, which is to be determined. A larger concentration of a weak scatterer (e.g., 1 monolayer of oxygen) or else a stronger scatterer (heavier adsorbate) would make the experiment more sensitive. For every material suitable edges have to be chosen, and it is not possible to give a general prescription.

ACKNOWLEDGMENTS

One of us (D.D.V.) acknowledges the hospitality of the Eidgenössiche Technische Hochschule–Zürich during his visits. The authors thank D. Celier and J.-M. Zisa of Riber Division, Instruments S.A. for their valuable advice in installing and operating the Mac-2 energy analyzer. This work is partly supported by the Schweiz-

erischer Nationalfonds zur Förderung der wissenschaftlichen Forschung. Computer time on the Cray Research Inc. X-MP/28 supercomputer provided by the Eidgenössische Technische Hochschule Rechenzentrum is gratefully acknowledged.

APPENDIX

To calculate the transition probability we begin with expression (1) in the main text:

$$W=\frac{2\pi}{\hbar}\sum_s |M_{E_s,p_s}^{E_{\rm inc},p_{\rm inc}}|^2\delta(E_{\rm inc}+E_i-E_f-E_s)\ .$$

Introducing the notation

$$M_{E_s,p_s}^{E_{\rm inc},p_{\rm inc}}=\langle i,{\rm inc}|V|f,s\rangle$$

for the matrix element, and

$$\langle \mathbf{r}_1,\mathbf{r}_2|f,s\rangle=\psi_s(\mathbf{r}_1)\psi_f(\mathbf{r}_2)\ ,$$

$$\langle s,f|\mathbf{r}_2',\mathbf{r}_1'\rangle=\psi_s^*(\mathbf{r}_1')\psi_f^*(\mathbf{r}_2')$$

for the final states, the transition rate W can be written as

$$\begin{aligned}W&=\frac{2\pi}{\hbar}\sum_s\langle i,{\rm inc}|V|f,s\rangle\langle s,f|V|{\rm inc},i\rangle\delta(E_{\rm inc}+E_i-E_f-E_s)\\&=\frac{2\pi}{\hbar}\langle i,{\rm inc}|V\left[\sum_s|f,s\rangle\langle s,f|\right]V|{\rm inc},i\rangle\delta(E_{\rm inc}+E_i-E_f-E_s)\\&=\frac{2\pi}{\hbar}\langle i,{\rm inc}|V|\mathbf{r}_2,\mathbf{r}_1\rangle\left[\sum_s\langle \mathbf{r}_1,\mathbf{r}_2|f,s\rangle\langle s,f|\mathbf{r}_2',\mathbf{r}_1'\rangle\delta(E_{\rm inc}+E_i-E_f-E_s)\right]\langle \mathbf{r}_1',\mathbf{r}_2'|V|{\rm inc},i\rangle\ ,\end{aligned}$$

where an integration over $\mathbf{r}_1$, $\mathbf{r}_2$, $\mathbf{r}_1'$, and $\mathbf{r}_2'$ is implied. Using the well-known expansion of the Green's function in terms of a complete set of states

$$\begin{aligned}G^+(\mathbf{r},\mathbf{r}';E)&=\lim_{\epsilon\to0}\sum_s\frac{\psi_s(\mathbf{r})\psi_s^*(\mathbf{r}')}{E-E_s+i\epsilon}\\&={\rm P}\sum_s\frac{\psi_s(\mathbf{r})\psi_s^*(\mathbf{r}')}{E-E_s}-i\pi\sum_s\psi_s(\mathbf{r})\psi_s^*(\mathbf{r}')\delta(E-E_s)\ ,\end{aligned}$$

where P denotes the principal part, we have

$$\begin{aligned}\sum_s\langle \mathbf{r}_1,\mathbf{r}_2|f,s\rangle\langle s,f|\mathbf{r}_2',\mathbf{r}_1'\rangle\delta(E_{\rm inc}+E_i-E_f-E_s)&=\psi_f(\mathbf{r}_2)\sum_s\psi_s(\mathbf{r}_1)\psi_s^*(\mathbf{r}_1')\delta(E_{\rm inc}+E_i-E_f-E_s)\psi_f^*(\mathbf{r}_2')\\&=\psi_f(\mathbf{r}_2)\left[-\frac{1}{\pi}\,{\rm Im}G^+(\mathbf{r}_1,\mathbf{r}_1';E_{\rm inc}+E_i-E_f)\right]\psi_f^*(\mathbf{r}_2')\ ,\end{aligned}$$

where $G^+(\mathbf{r}_1,\mathbf{r}_1';E)$ is the Green's function at energy E of the scattering photoelectron, W becomes

$$W=-\frac{2}{\hbar}\int d\mathbf{r}_1\cdots\int d\mathbf{r}_2'\,\psi_i^*(\mathbf{r}_1)\psi_{\rm inc}^*(\mathbf{r}_2)V\psi_f(\mathbf{r}_2){\rm Im}G^+(\mathbf{r}_1,\mathbf{r}_1';E_{\rm inc}+E_i-E_f)\psi_f^*(\mathbf{r}_2')V\psi_{\rm inc}(\mathbf{r}_2')\psi_i(\mathbf{r}_1')\ .$$

If the initial and final states of the primary electron are taken as plane waves,

$$\psi_{\rm inc}=e^{i\mathbf{q}_i\cdot\mathbf{r}},\quad \psi_f=e^{i\mathbf{q}_f\cdot\mathbf{r}}\ ,$$

we finally obtain

$$W=-\frac{2}{\hbar}\int d\mathbf{r}_1\cdots\int d\mathbf{r}_2'\,\psi_i^*(\mathbf{r}_1)\frac{1}{|\mathbf{r}_1-\mathbf{r}_2|}e^{i(\mathbf{q}_f-\mathbf{q}_i)\cdot\mathbf{r}_2}{\rm Im}G^+(\mathbf{r}_1,\mathbf{r}_1';E_{\rm inc}+E_i-E_f)e^{-i(\mathbf{q}_f-\mathbf{q}_i)\cdot\mathbf{r}_2'}\frac{1}{|\mathbf{r}_1'-\mathbf{r}_2'|}\psi_i(\mathbf{r}_1')\ .$$

*Present address: Institute for Materials Research, McMaster University, Hamilton, Ontario, Canada L8S 4M1.

†Permanent address: The Blackett Laboratory, Imperial College of Science and Technology, University of London, London SW7 2BZ, United Kingdom.

[1]J. B. Pendry, *Low Energy Electron Diffraction* (Academic, London, 1974).

[2]H. R. Moser, Ph.D. dissertation, Eidgenössische Technische Hochschule–Zürich, 1983; F. P. Netzer, G. Strasser, and J. A. D. Matthew, Phys. Rev. Lett. **51**, 211 (1983).

[3]J. A. D. Matthew, G. Strasser, and F. P. Netzer, Phys. Rev. B **27**, 5839 (1983).

[4]*Giant Resonances in Atoms, Molecules, and Solids*, edited by J. P. Connerade, J. M. Esteva, and R. C. Karnatak (Plenum, New York, 1987).

[5]P. Auger, Compt. Rend. (Paris) **177**, 169 (1923).

[6]U. Fano, Phys. Rev. **124**, 1866 (1961).

[7]*EXAFS Spectroscopy: Techniques and Applications*, edited by B. K. Teo and D. Joy (Plenum, New York, 1981).

[8]M. De Crescenzi and G. Chiarello, J. Phys. C **18**, 3595 (1985).

[9]P. A. Lee, P. H. Citrin, P. Eisenberger, and B. M. Kincaid, Rev. Mod. Phys. **53**, 769 (1981).
[10]W. E. Ekardt and D. B. Tran Thoai, Solid State Commun. **45**, 1083 (1983).
[11]F. Combet Farnoux and A. P. Hitchcock, Solid State Commun. **64**, 961 (1987).
[12]B. K. Teo and P. A. Lee, J. Am. Chem. Soc. **101**, 2815 (1979).
[13]D. B. Tran Thoai, A. Santoni, W. Ekardt, and J. Urban, Solid State Commun. **58**, 315 (1986).
[14]F. W. Lytle, D. E. Sayers, and E. A. Stern, Phys. Rev. B **15**, 2426 (1977).
[15]P. Rabe, G. Tolkiehn, and A. Werner, J. Phys. C **12**, 899 (1979).
[16]M. Fanfoni, S. Modesti, N. Motta, M. DeCrescenzi, and R. Rosei, Phys. Rev. B **32**, 7826 (1985).
[17]L. F. Mattheiss, Phys. Rev. **133**, A1399 (1964).
[18]F. Herman and S. Skillman, *Atomic Structure Calculations* (Prentice Hall, Engelwood Cliffs, NJ, 1965).
[19]E. Clementi and C. Roetti, in *Atomic Data and Nuclear Data Tables* (Academic, New York, 1974), Vol. 14, p. 177.
[20]J. C. Slater, Phys. Rev. **81**, 385 (1951).
[21]D. K. Saldin, Phys. Rev. Lett. **60**, 1197 (1988).
[22]V. I. Ochkur, Zh. Eksp. Theor. Fiz. **47**, 1746 (1964) [Sov. Phys.—JETP **20**, 1175 (1965)].
[23]V. I. Ochkur, Zh. Eksp. Theor. Fiz. **45**, 734 (1963) [Sov. Phys.—JETP **18**, 503 (1964)].
[24]N. F. Mott and H. S. W. Massey, *The Theory of Atomic Collisions* (Clarendon, Oxford, 1965).
[25]P. J. Durham, J. B. Pendry, and C. H. Hodges, Comput. Phys. Commun. **25**, 193 (1982).
[26]J. S. Faulkner and G. M. Stocks, Phys. Rev. B **21**, 3222 (1980).
[27]A. Šimunek, O. Šipr, and J. Vackář, Phys. Rev. Lett. **63**, 2076 (1989).
[28]D. D. Vvedensky, D. K. Saldin, and J. B. Pendry, Comput. Phys. Commun. **40**, 421 (1986).
[29]R. D. Leapman, P. Rez, and D. F. Mayers, J. Chem. Phys. **72**, 1232 (1980).
[30]P. Schattschneider, *Fundamentals of Inelastic Electron Scattering* (Springer, Vienna, 1986).
[31]R. E. Dietz and G. McRae, Phys. Rev. B **21**, 2229 (1980).
[32]F. Combet Farnoux, Z. Phys. D **2**, 327 (1986).
[33]W. Speier, J. C. Fuggle, R. Zeller, and M. Campagna, in *EXAFS and Near Edge Structure III*, edited by K. O. Hodgson, B. Hedman, and J. E. Penner-Hahn (Springer, New York, 1984), p. 496.
[34]P. O. Nilsson and C. G. Larsson, Phys. Rev. B **27**, 6143 (1983).
[35]R. D. Leapman, L. A. Grunes, and P. L. Fejes, Phys. Rev. B **26**, 614 (1982).
[36]A. P. Hitchcock and C. H. Teng, Surf. Sci. **149**, 558 (1985).
[37]S. Kiyono, S. Chiba, Y. Hayashi, S. Kato, and S. Mochimaru, Jpn. J. Appl. Phys. **17**, Suppl. 2, 212 (1978).
[38]P. Aebi, M. Erbudak, F. Vanini, and D. D. Vvedensky (unpublished).
[39]E. Dartyge, A. Fontaine, G. Tourillon, R. Cortes, and A. Jucha, Phys. Lett. **113A**, 384 (1986).
[40]H. H. Madden, D. M. Zehner, and J. R. Noonan, Phys. Rev. B **17**, 3074 (1978).